The study on the high-temperature performances of a graphene MEMS pressure sensor

Daosen Liu[1,2,*] , Shengsheng Wei[1], Chao Liu[2], and Dejun Wang[1]

[1] *Faculty of Electronic Information and Electrical Engineering, Liaoning Key Lab of Integrated Circuit and Biomedical Electronic System, Dalian University of Technology, Dalian 116024, China*
[2] *Communication and Electronic Engineering Institute, Qiqihar University, Qiqihar 161006, China*

ABSTRACT

A sensitive element for realizing the pressure sensing at high temperature is experimentally prepared using the microelectromechanical systems (MEMS) fabrication technology and consists of a 50-µm-thick, 1400-µm-wide square multilayer component membrane (including silicon, silicon dioxide, and silicon nitride) and a monolayer graphene with meander pattern. The prepared sample is characterized and analyzed using various techniques including atomic force microscopy, Raman spectroscopy, and the finite element method. The strain distribution in the pressed membrane is simulated by the finite element method. The pressure sensing based on the monolayer graphene with meander pattern can be realized according to the strain distribution and the high-temperature measurements for the sensitive element. Accordingly, a new pressure sensor based on the sensitive element is proposed for exploring the sensing performance depending on the piezoresistive property of monolayer graphene at high temperature. The sensing performance can be obtained by the theoretical analysis for electromechanical measurements at high temperature for the sensitive element. The results demonstrate that the performances of the sensor are excellent at high temperature. In particular, the sensitivity is much higher than that of previous high-temperature MEMS pressure sensors. Our results can provide insights for realizing the high-temperature applications of graphene in electronic devices.

1 Introduction

There is a wide demand for high-temperature pressure sensors in harsh environments such as the automotive industry, aerospace industry, and chemical processing. The researches on high-temperature pressure sensors have attracted a lot of scientific interests and become significant topics. At present, the mainstream technology for studying high-temperature pressure sensors is the silicon-on-insulator (SOI) technology, which requires the introduction of an insulating layer between silicon and the substrate

---

and uses silicon as the sensitive material. The SOI high-temperature pressure sensors have the advantages of high temperature resistance, radiation resistance, high cost performance and so on, but the sensors are not very stable at high temperature and self-heating is a problem [1–4]. The point is that the sensitivity is at a conventional level. In addition, silicon carbide is a high-temperature-resistant semiconductor material. The pressure sensor based on silicon carbide has higher temperature tolerance than the SOI pressure sensor, but its sensitivity is not superior to that of the SOI pressure sensor [5].

Graphene is the most robust and flexible material at present. A number of excellent properties have been found theoretically and experimentally. For example, the high carrier mobility and thermal conductivity have been acquired and, respectively, reach up to 200,000 cm^2/Vs [6, 7] and 5×10^3 W/mK [8] for suspended graphene membranes. These excellent features have the potential to improve the response speed and heat dissipation of electronic devices. Particularly, it has been confirmed that graphene has a higher gauge factor than semiconductors [9]. It indicates that graphene is more sensitive than semiconductors such as silicon. Therefore, it can be predicted that the sensitivity of high-temperature pressure sensor based on graphene is higher than that of semiconductor-based high-temperature pressure sensor [10].

To verify the high-temperature performance of graphene pressure sensor, a graphene MEMS pressure sensor with a Wheatstone bridge circuit formed from several graphene resistances integrated on a chip has been proposed in this paper. The sensing performances of the sensor at high temperature are obtained by the theoretical analysis for electromechanical measurements for the only monolayer graphene resistance as sensitive element. The results demonstrate that the performances of the sensor are excellent at high temperature. In particular, the sensitivity which can be up to 10^{-4} /kPa orders of magnitude is much higher than that of previous high-temperature MEMS pressure sensors. Our results can provide insights for realizing the high-temperature applications of graphene in electronic devices.

2 Materials and methods

2.1 Device fabrication

The research group purchased a 0.5-mm-thick commercial single-crystal silicon wafer and a Trivial Transfer Graphene from ACS Material, Nanjing XFNANO Materials Tech Co., Ltd. (XFNANO), which is a monolayer graphene with polymethyl methacrylate (PMMA).

Devices need to be fabricated by the standard techniques. First, the silicon wafer was thermally oxidized for the electrical isolation, and the silicon nitride membrane was deposited onto the oxide with the thickness of 200 nm. Its thickness is about 100 nm. Next, 50 nm of Cr and 250 nm of Au were evaporated to the silicon nitride layer for realizing the contact. The electrode patterning was obtained by the use of photolithography and chemical etching. Again, it is very pivotal that the devices have the electromechanical sensing. To this end, 1400-μm-wide square cavities were defined by photoresist and etched 450.3 μm deep into the silicon layer at the wafer backside. Then, the wafer backside was bonded with a piece of glass for sealing gas in the cavities, which can form pressure difference inside and outside them. In the end, the monolayer graphene need to be transferred onto the above-mentioned substrate. The graphene/PMMA was rinsed in deionized water and the substrate picked up it. In order to let the graphene adhere to the silicon nitride layer, the chip was baked for 20 min at 100 °C. The PMMA was then dissolved by acetone, followed by ethyl alcohol rinsing. The graphene patterning was defined by photolithography and etched using an O_2 plasma process after the chip was again baked for 10 min at 50 °C in order to dry the graphene.

2.2 Material characterization

In recent years, atomic force microscope and Raman spectrometer have become powerful characterization and metrology tools for solid materials at the nanoscale. These tools need to be employed for verifying the quality of graphene on the device. The atomic force microscope and the Raman spectrometer can, respectively, detect the roughness and the layer number of graphene.

2.3 Simulation

In order to obtain the gauge factor of graphene, the strain of the cavity membrane was analyzed by COMSOL finite element method. The whole x-direction strains on the cavity membrane were simulated when the pressure difference with 0.1 MPa was loaded to this membrane. Meanwhile, the strain data on the cavity membrane with different loads from 0.1 to 0.5 MPa were extracted and analyzed, respectively.

2.4 Measurement

A MENSOR pressure controller was employed and can output the gas pressure. The controller can directly indicate the pressure value. Argon was used and the positive gas pressure can be loaded to a device when it worked, which can cause pressure difference inside and outside its cavity. The sensing of the device is realized because of the bending of the pressed cavity membrane resulting in the graphene deformation. Multimeter combined with the pressure controller was applied in order to obtain the electromechanical measurement data at high temperature.

3 Results and discussion

3.1 Fabrication and characterization

Figure 1 shows the schematic of device. The membrane above the cavity of device, which is multilayer component membrane, is used as the structural element and consists of silicon and silicon dioxide and silicon nitride (SiNx). As shown in Fig. 1a, the membrane above the cavity is poised when it is not disturbed by outside factors. This is because the pressure inside and outside the sealed cavity is the same. Figure 1b shows the schematic of the pressed device. It can be seen that P_0 and P are, respectively, the pressures inside and outside the cavity. When P is greater than P_0, the membrane deforms and forms a concave shape.

Figure 2a shows the manufacturing process of the devices. As expounded in the section of device fabrication method, the process includes oxidizing, depositing, evaporating, etching, bonding, and imaging graphene. The lateral view of Fig. 2a provides the device structure at each step of the process, and the top view of Fig. 2a shows the morphology of graphene on SiNx film after O_2 plasma etching. From the top view, it can be seen that the only monolayer graphene resistance has the meander pattern. The graphene resistance as sensitive element is above the cavity. Figure 2b shows the characterization of graphene on the device. Although the micrograph indicates that few pollutants are on the graphene surface, the graphene is smooth. From the Raman spectrum, it can be seen that the monolayer graphene is verified and the few defects are in the graphene.

3.2 Piezoresistive effect

In order to get the deformation of the suspended membrane above the sealed cavity shown in Fig. 1, the COMSOL simulation was performed. The whole strains in the x-direction are shown in Fig. 3 when the pressure difference with 0.1 MPa was loaded to this membrane. From Fig. 3, we can observe that there are not only tensile distortions but also compressive distortions on the edge of the membrane. The only graphene resistor in Fig. 2a was placed at the compression region (marked with either black arrow) for exploring the sensing character of the graphene contracted by the compressible deformation of the substrate. When the pressure differences of 0.1–0.5 MPa were, respectively, loaded to the cavity membrane, the strain data at the compression region were correspondingly extracted and analyzed as shown in Fig. 4. The averaged strains at the compressive region (marked with black arrow in Fig. 3) are shown in Fig. 4a. It can be seen that the averaged strain linearly increases as the pressure increases

Fig. 1 The schematic of device: (a) the basic structure of device; (b) the status of device under the applied differential pressure
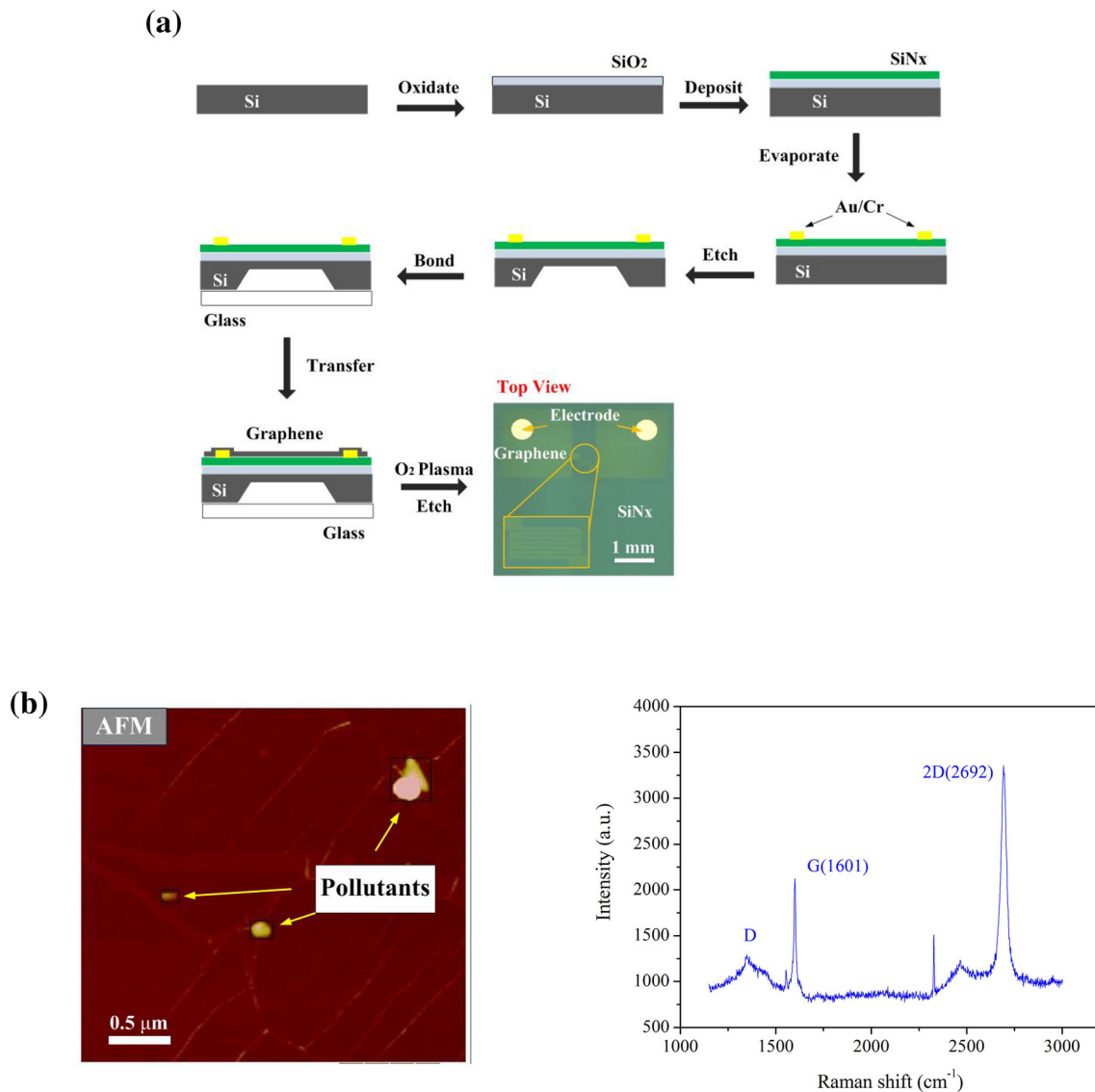
(a)

(b)
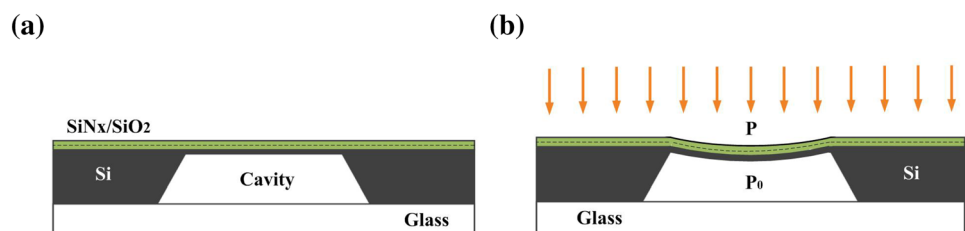
Fig. 2 Preparation and characterization of device: (**a**) the technological process for fabricating devices; (**b**) the atomic force micrograph and the Raman spectrum of graphene
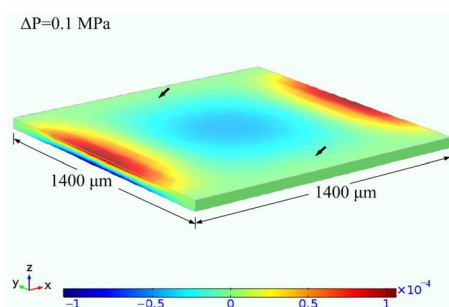

Fig. 3 Simulative ε_{xx} strain distribution under the differential pressure with 0.1 MPa for cavity membrane

gradually. In order to obtain the high-temperature performances of the device, the measurements at 200 °C were subsequently performed for the sample. As shown in Fig. 4a, the relative changes of the only graphene resistance are negative, which indicates that the resistance decreases as the graphene is compressed in the plane. The relative change has the nonlinear growth as the pressure increases gradually. The gauge factor of the compressible graphene was analyzed by the expression of $G = \Delta R / R\varepsilon$. Figure 4b indicates that the gauge factor of the compressible graphene is enormous at high temperature, and it has
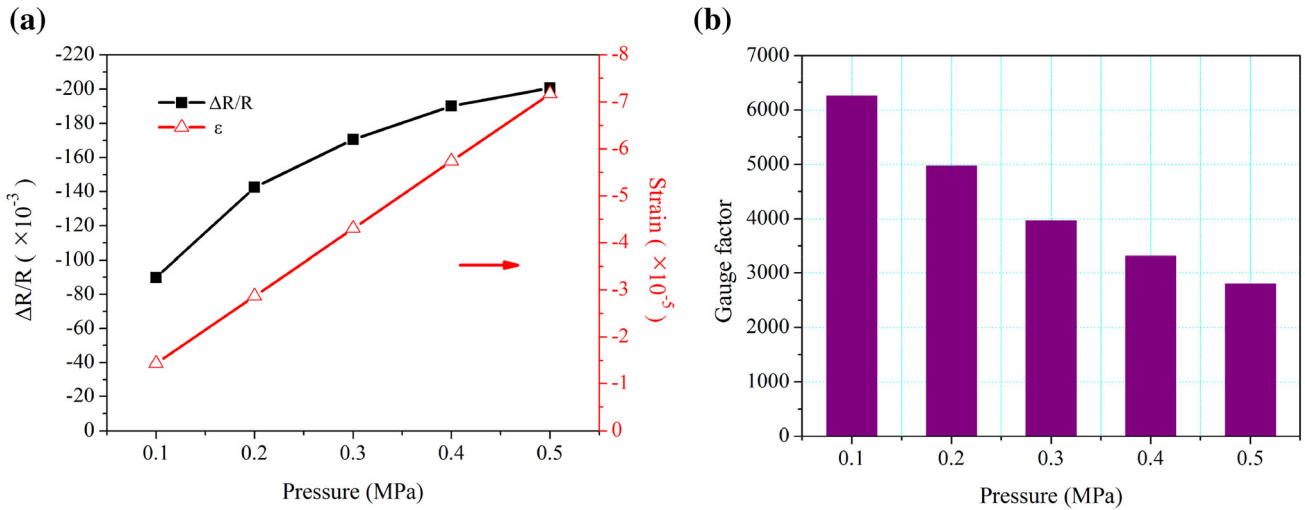
Fig. 4 The in-plane compressible character of graphene: (**a**) the relative changes of single graphene resistance; (**b**) the gauge factors of graphene at 200 °C

the nonlinear decline as the pressure increases gradually.

3.3 Electromechanical characterizations

In order to further know the high-temperature performances of the device, a new pressure sensor which is based on the above sensitive element is proposed and shown in the illustration (1) in Fig. 5. From the illustration, it can be seen that the sensor includes four graphene resistances. They have the meander patterns and are symmetric to the device center. Their original resistances are equal because every meander pattern is identical to the one of only monolayer graphene resistance shown in Fig. 2a. Therein, a pair of graphene resistors, which act as sensitive units, sit above the cavity, but the rest is not above the cavity and keeps constant. A DC power supply and a multimeter can be connected to the above circuit according to the illustration (2) in Fig. 5 so that a Wheatstone bridge based on the monolayer graphene with meander patterns is formed. The R in the illustration represents single graphene resistance as sensitive unit, and the R_0 represents constant graphene resistance. The voltage output ΔV in the Wheatstone bridge can be expressed as formula (1), the U of which is the DC source voltage.

$$\Delta V = 2UR_0/(R_0 + R) - U \tag{1}$$

The electromechanical properties of the proposed sensor can be acquired by the combination of high-temperature measurements for the only monolayer
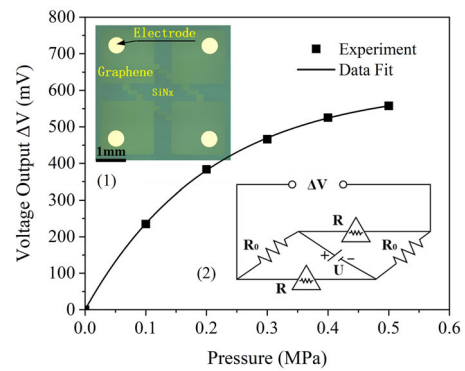

Fig. 5 Voltage output with the range of 0 to 0.5 MPa at 200 °C

graphene resistance as sensitive unit in Fig. 2a and theoretical analysis by formula (1) for this sensor [11]. From Fig. 5, the derived data at 5 V obtained from the experiment at 200 °C show that the voltage output increases nonlinearly as the differential pressure rises in the range of 0 to 0.5 MPa. From Fig. 6a, the derived data at 5 V obtained from the experiment at 200 °C, 220 °C, and 240 °C show that the variations of voltage outputs are largely linear as the differential pressures rise in the range of 0 to 100 kPa. Figure 6a shows that the sensitivity of the sensor is different at different high temperatures. The sensitivity is about 3.51×10^{-4} /kPa at 200 °C. The sensitivity is about 2.23×10^{-4} /kPa at 220 °C. The sensitivity is about 2.94×10^{-4} /kPa at 240 °C. From the sensitivity comparison among high-temperature MEMS pressure sensors in Table 1, it can be seen that its sensitivity is better than that of previous sensors. At the

same time, the fitting curves for every group data are presented in Fig. 5 and Fig. 6a. Overall, the sensor can maintain linear and stable operation in the range of 0–100 kPa at each high temperature.

A single cycle can illustrate the sensor's response process, overall response rate, and recovery rate, and more cycles can further confirm the reversibility of the sensor. Therefore, more cyclic tests were performed at each high temperature in order to demonstrate the reversibility of the sensor. The more cyclic tests for the sensor at high temperature were obtained by switching the pressure in 3 cycles of ON/OFF test for the device in Fig. 2a. Each switching cycle was performed by turning controller on/off with fixed differential pressure. While turning off the controller, the cavity membrane was apace relaxed due to the rapid venting from the gas line. It followed that the voltage output fell quickly. From Fig. 6, it can be seen that the sensor has good reversibility at each

high temperature. It should be noted that the fluctuations marked by circles in Fig. 6b were likely to be caused by external factors such as vibration. Figure 6c shows the multiple pressurization tests of 60 kPa at 220 °C. The dynamic voltage outputs caused by these pressurization tests are similar. The differences between the voltage output peaks obtained by the multiple pressurization tests are about 4.3, 3.0 and 1.4%. Figure 6(d) shows the multiple pressurization tests of 60 kPa at 240 °C. The multiple pressurization tests at this high temperature also show similar dynamic output characteristics. The differences between the voltage output peaks obtained by the multiple pressurization tests are about 4.8%, 0.6%, and 5.2%. It can be seen that the difference in voltage output obtained by repeating the identical test at high temperature is lower. The temperature gradient test shows that the sensor can operate stably at high temperature.
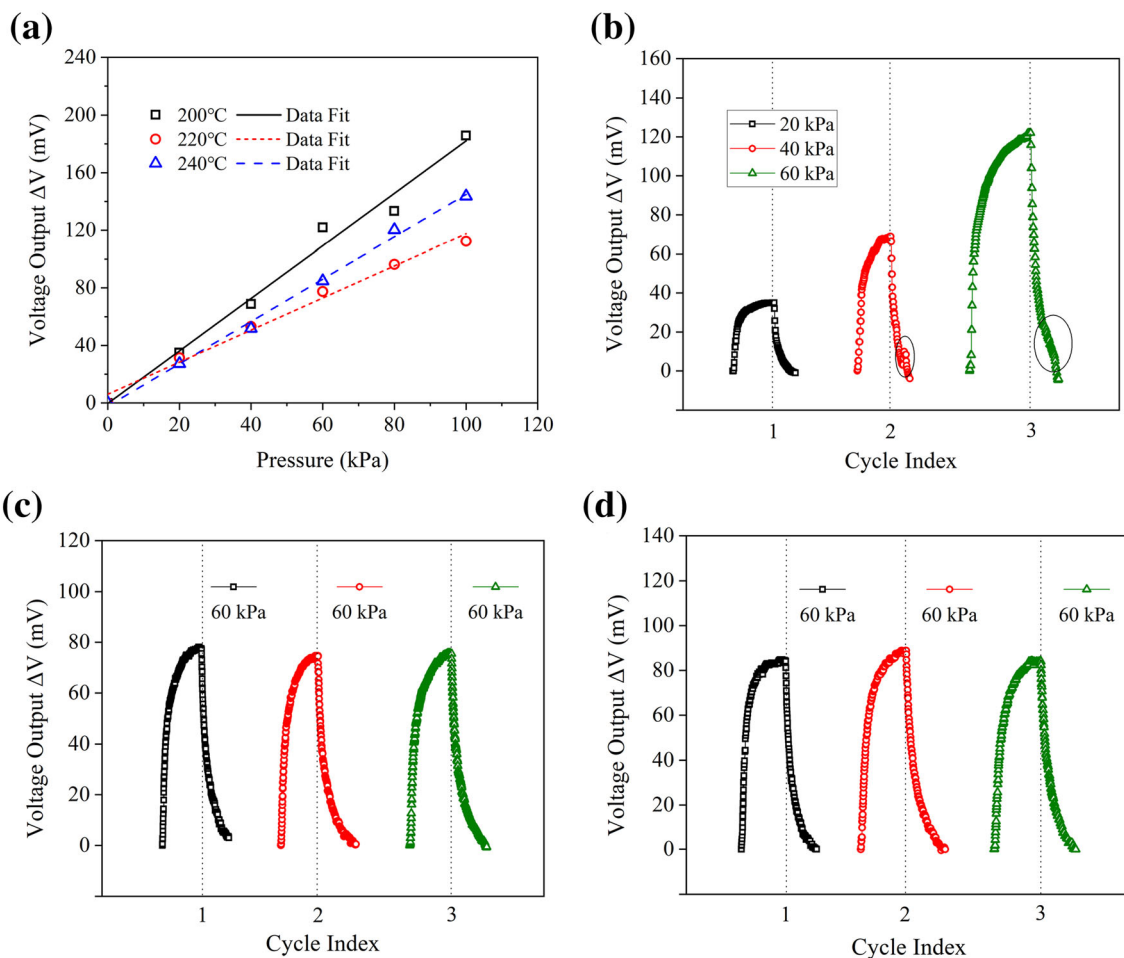

Fig. 6 Voltage output: (**a**) in the range of 0 to 100 kPa; (**b**) for cycling test at 200 °C; (**c**) for cycling test at 220 °C; (**d**) for cycling test at 240 °C

Table 1 Sensitivity comparison among high-temperature MEMS pressure sensors

Group	Yao [1]	Zhao [2]	Li [3]	Li [4]	Yang [5]	This paper
Material	SOI	SOI	SOI	SOI	SiC	Monolayer graphene
Sensitivity (kPa^{-1})	2.1×10^{-4}	2.48×10^{-6}	2.67×10^{-5}	6.67×10^{-6}	1.67×10^{-6}	$(2.23$–$3.51) \times 10^{-4}$
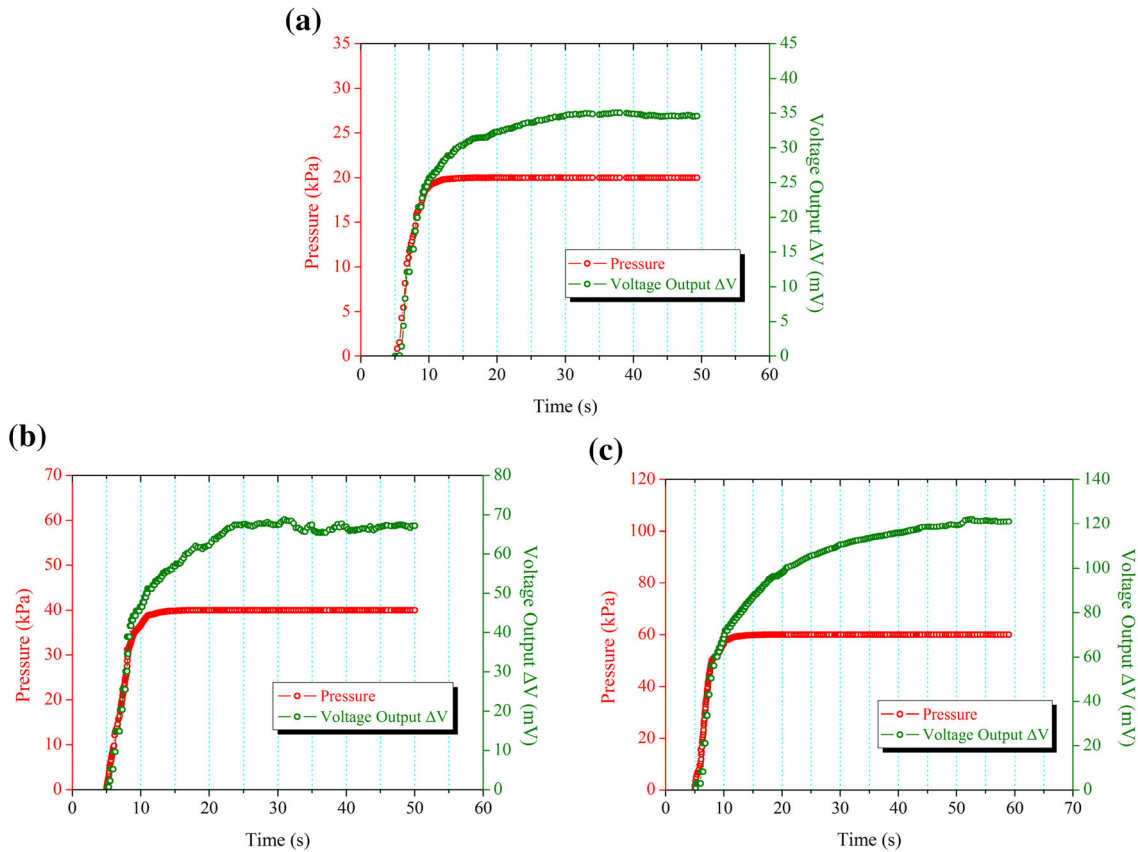
Fig. 7 Dynamic response of voltage output with differential pressure at 200 °C: (**a**) under the condition of the pressure with 20 kPa; (**b**) under the condition of the pressure with 40 kPa; (**c**) under the condition of the pressure with 60 kPa

In order to know the dynamic response of the sensor at high temperature, the pressed courses are shown in Fig. 7. Since the dynamic response at various high temperatures has similar characteristics, only the dynamic response at 200 °C is shown in Fig. 7. The voltage output quickly rises as the pressure changes. The voltage output is exactly the same as the pressurization process. The hysteresis phenomena between the voltage output and the pressure are not almost seen during the rising of the pressure. Nevertheless, the voltage output does not reach the peak value when the pressure just rises to the constant. With the subsequent pressure remaining constant, the output voltage gradually stabilizes after a slight rise and fall. The hysteresis phenomena are probably caused by the inertia and size effect of the cavity membrane and the thermal effect of high temperature. When the pressure is just constant, the inertial cavity membrane will continue to operate for some time before returning to the equilibrium position. Furthermore, the size and temperature effects increase the risk of creep and plastic deformation of the cavity membrane [12–14], which is likely to result in strain lag–stress for the cavity membrane [15]. Taking into account the complex effects of various factors including inertia, size, and temperature, the
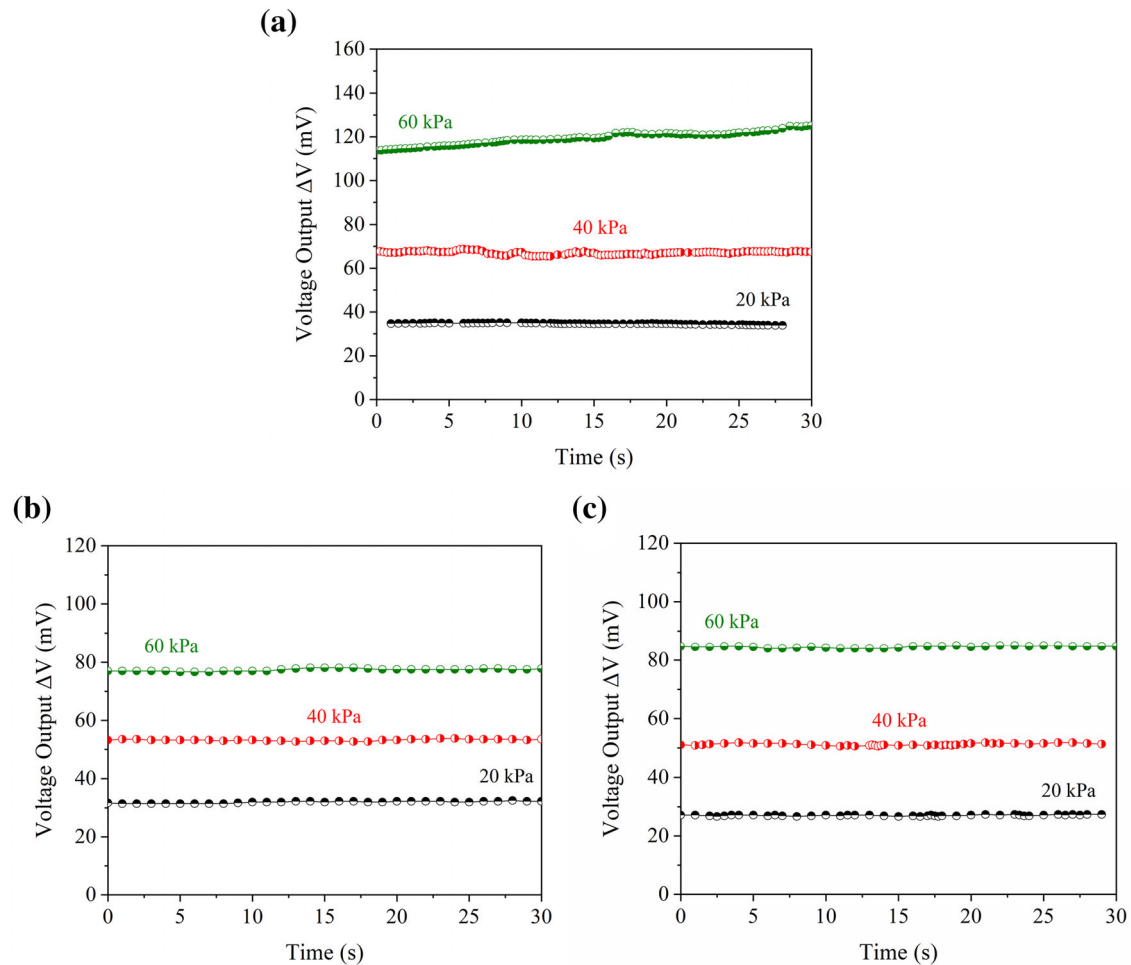
Fig. 8 Voltage output under differential pressure with step increase from 20 to 60 kPa (20 kPa per step): (**a**) T = 200 °C; (**b**) T = 220 °C; (**c**) T = 240 °C

output voltage will rise and fall slightly for longer time at the initial stage of pressure remaining, which is consistent with expectation. At the same time, the fluctuation happens during tending to be stable for the voltage output. As shown in Fig. 7, the fluctuation of the voltage output for the pressure with 40 kPa is bigger than the others.

The high-temperature measurements on pressure maintaining were also made at different differential pressures across the cavity membrane as indicated in Fig. 8. The voltage outputs rise in different steps as the compressive strains applied to the graphene resistances acting as sensitive elements are strengthened. These steps indicate that the piezoresistive effect of graphene is well responsive to the deformation of the membrane. As shown in Fig. 8, the effect of the pressure maintaining is well for every step at each high temperature though there are slight fluctuations for the voltage outputs in most steps.

4 Conclusion

In summary, we use the MEMS standard technology to propose a pressure sensor based on the in-plane compressible character of monolayer graphene and study emphatically its high-temperature performances. The results show that the sensitivity of the proposed sensor can reach up to 10^{-4} /kPa orders of magnitude at high temperature, which indicates that it is more sensitive than previous MEMS pressure sensors. Simultaneously, the dynamic performances present the well response of the piezoresistive effect of monolayer graphene to gas pressure at high temperature. Our study can provide certain reference for

realizing the high-temperature applications of graphene devices.

Author contributions

DL: contributed to conceptualization, methodology, formal analysis and investigation, and writing—original draft preparation. DL and SW: contributed to writing—review and editing. DL and CL: contributed to funding acquisition. DW: contributed to resources and supervision.

Data availability

All data generated or analyzed during this study are included in this published article.

Declarations

Conflict of interest The authors have no relevant financial or non-financial interests to disclose.

References

1. Z. Yao, T. Liang, P. Jia, Y. Hong, L. Qi, C. Lei, B. Zhang, J. Xiong, Sensors (2016). https://doi.org/10.3390/s16060913

2. Y. Zhao, L. Zhao, Z. Jiang, Sensors and Actuators A (2003). https://doi.org/10.1016/j.sna.2003.07.011

3. S. Li, T. Liang, W. Wang, Y. Hong, T. Zheng, J. Xiong, Journal of Semiconductors (2015). https://doi.org/10.1088/1674-4926/36/1/014014

4. X. Li, Q. Liu, S. Pang, K. Xu, H. Tang, C. Sun, Sensors and Actuators A (2012). https://doi.org/10.1016/j.sna.2012.03.027

5. J. Yang, Sensors (2013). https://doi.org/10.3390/s130302719

6. K.I. Bolotin, K.J. Sikes, Z. Jiang, M. Klima, G. Fudenberg, J. Hone, P. Kim, H.L. Stormer, Solid State Commun (2008). https://doi.org/10.1016/j.ssc.2008.02.024

7. S.V. Morozov, K.S. Novoselov, M.I. Katsnelson, F. Schedin, D.C. Elias, J.A. Jaszczak, A.K. Geim, Phys Rev Lett (2008). https://doi.org/10.1103/PhysRevLett.100.016602

8. A.A. Balandin, S. Ghosh, W. Bao, I. Calizo, D. Teweldebrhan, F. Miao, C.N. Lau, Nano Letters (2008). https://doi.org/10.1021/nl0731872

9. X. Chen, J Vacuum Sci Technol B, Nanotechnol Microelectron (2011). https://doi.org/10.1116/1.3660784

10. H.Y. Nan, Z.H. Ni, J. Wang, Z. Zafar, Z.X. Shi, Y.Y. Wang, J Raman Spectrosc (2013). https://doi.org/10.1002/jrs.4312

11. R. Nakagawa, Z. Wang, K. Suzuki, Proceedings of the ASME 2018 International Mechanical Engineering Congress and Exposition (2018). https://doi.org/10.1115/IMECE2018-87277

12. J. Ren, M. Ward, P. Kinnell, R. Craddock, X. Wei, Sensors (2016). https://doi.org/10.3390/s16020204

13. J. Thurn, R.F. Cook, J Appl Phys (2002). https://doi.org/10.1063/11432773

14. L. Huang, Z. Ding, J. Yuan, D. Zhou, Z. Yin, Ceram Int (2022). https://doi.org/10.1016/j.ceramint.2021.12.104

15. S. Fan, L. Meng, L. Dan, W. Zheng, X. Wang, IEEE Sens J (2018). https://doi.org/10.1109/JSEN.2018.2877747